Electroweak precision constraints of the 2HDM+S*

Cheng Li (李成)[1†] Juxiang Li (李菊香)[1‡] Shufang Su[2§] Wei Su (苏伟)[1,3¶]

[1]School of Science, Shenzhen Campus of Sun Yat-sen University, Guangming District, Shenzhen 518107, China
[2]Department of Physics, University of Arizona, Tucson, AZ 85721, USA.
[3]Institute of Theoretical Physics, Chinese Academy of Sciences, Beijing 100190, China

Abstract: The 2HDM+S is the singlet extension of the two-Higgs-doublet model (2HDM). The singlet field and its mixing with the 2HDM Higgs sector lead to new contributions to the electroweak precision observables, in particular, the oblique parameters. In this study, we performed a systematic investigation of the impacts of each mixing angle on the oblique parameters. We adopted the mixing angles and physical Higgs masses as our parameters, which allow a mapping when a specific symmetry structure of the Higgs potential and various theoretical considerations are taken into account. We identified five benchmark cases, where at most one mixing angle was nonzero, and analyzed the 95% C.L. allowed parameter space using the oblique parameters. In the alignment limit of the 2HDM, we find that, other than the usual mass relations of $m_H \sim m_{H^\pm}$ or $m_A \sim m_{H^\pm}$, electroweak precision measurements also impose an upper limit on the neutral Higgs masses. In the cases with nonzero singlet mixing with the 2HDM Higgses H or A, we find approximate mass relations of $c^2_{\alpha_{HS}} m_H + s^2_{\alpha_{HS}} m_{h_S} = m_{H^\pm}$ or $c^2_{\alpha_{AS}} m_A + s^2_{\alpha_{AS}} m_{A_S} = m_{H^\pm}$. These relations are universal to the 2HDM+S models, with or without further symmetry assumption. We also studied the non-alignment limit of the 2HDM+S, which typically has tighter constraints on the masses and mixing angles. Finally, we examined the complementarity between the electroweak precision analyses and the Higgs coupling precision measurements.

Keywords: electroweak precision observables, extended Higgs sector, oblique parameters

DOI: 10.1088/1674-1137/ae24e6 **CSTR:** 32044.14.ChinesePhysicsC.50023105

I. INTRODUCTION

Electroweak precision observables have provided a precise test of the standard model (SM) at the loop level [1, 2], which is consistent with the observations of a 125 GeV SM-like Higgs [3, 4]. However, the SM could not provide satisfactory solutions to dark matter, neutrino mass, baryogenesis, etc. [5−8]. Furthermore, the naturalness problem in the SM points to new physics beyond the SM [9].

One of the simplest extensions of the SM Higgs sector is the two-Higgs doublet model (2HDM) [10], which has been studied extensively. The 2HDM can be further extended by an additional singlet field, which is the N2HDM with a real singlet [11−13], and the 2HDM+S with a complex singlet [14, 15]. The 2HDM+S matches the next-to minimal supersymmetric standard model (NMSSM) [16] at a low energy scale and can provide a dark matter candidate [17−19], as well as accommodate the possible 95 GeV excess at the LEP and LHC [15]. The phenomenological properties of the 2HDM+S have only been explored in some specific scenarios, whereas the more general cases of the 2HDM+S have not yet been studied in detail. In this study, we explore the implications of the electroweak precision measurements on the 2HDM+S parameter space. In particular, we focus on the oblique parameters S, T, and U, which are sensitive to the new physics contributions to the W and Z self-energies

Received 12 October 2025; Accepted 26 November 2025; Accepted manuscript online 27 November 2025

* Cheng Li, Juxiang Li, and Wei Su are supported by the Natural Science Foundation of China (NSFC) (12305115), Shenzhen Science and Technology Program (20220619300001, 20220816094256002), Guangdong Provincial Key Laboratory of Gamma-Gamma Collider and Its Comprehensive Applications (2024KSYS001), and Guangdong Provincial Key Laboratory of Advanced Particle Detection Technology (2024B1212010005). Juxiang Li is also supported by the Fundamental Research Funds for the Central Universities, and the Sun Yat-sen University Science Foundation. Shufang Su is supported by the Department of Energy (DEFG02-13ER41976/DE-SC0009913)

† E-mail: lich389@mail.sysu.edu.cn
‡ E-mail: lijx376@mail2.sysu.edu.cn
§ E-mail: shufang@email.arizona.edu
¶ E-mail: suwei26@mail.sysu.edu.cn (Corresponding author)

[20, 21].

The scalar sector of the 2HDM+S includes two $SU(2)_L$ doublets and a complex singlet. The singlet field does not couple to the SM gauge bosons and fermions. After the neutral components achieve vacuum expectation values (vev), assuming no CP-violation, the mass spectrum of the Higgs sectors includes 3 CP-even scalars, two CP-odd scalars, and a pair of charged Higgses. In particular, the CP-even and CP-odd singlet components mix with the corresponding ones in the $SU(2)_L$ doublets, which leads to the couplings of the singlet-like scalars to the SM gauge bosons, as well as modifications of the couplings of the doublet-like scalars to the SM sector. The most general 2HDM+S Higgs potential has 27 free parameters, and 11 of these can be chosen to be the masses of the Higgs bosons, as well as the mixing angles between Higgses. The remaining parameters in the Higgs potential are the Higgs self-couplings, which do not directly contribute to the oblique parameters. Therefore, in our study, we only focus on the *STU* constraint and the relevant parameters, including these 11 mass and mixing parameters. We parameterize such mixing parameters by α_{hS}, the mixing of the CP-even singlet with the 125 GeV SM-like Higgs h, α_{HS}, the mixing of the CP-even singlet with the 2HDM CP-even Higgs H, and α_{AS}, the mixing of the CP-odd singlet with the 2HDM CP-odd Higgs A.

While the general formalism for the contributions of various Higgses to the oblique parameter exists in literature [22], the analyses of electroweak precision constraints in the 2HDM+S could be complex given the enlarged parameter space. In our analyses, we performed a systematic study of the impacts of each mixing angle on the oblique parameters. Including the usual 2HDM mixing angle of the CP-even Higgses α, we introduce five basic benchmark scenarios, Case-0 for the 2HDM alignment limit and Cases-I−IV in which only one mixing angle is set to be nonzero. We analyze the contributions to the oblique parameters in each case and study the 95% C.L. allowed region in the relevant parameter spaces under the oblique parameters. After the discussion of these five benchmark scenarios, we discuss the cases with a non-zero singlet mixing angle away from the alignment limit.

The implications of electroweak precision measurements in the 2HDM and singlet extended SM have been studied in the literature [22−27]. Our study offers a comprehensive electroweak precision analysis of the 2HDM+S and identifies the impact of each singlet mixing angle. As only the couplings between the Higgses and the SM gauge bosons enter the oblique parameters, our results are universal to the 2HDM+S models, with or without further symmetry assumption of the Higgs potential. In addition, we explore the complementarity of the electroweak precision analyses with the Higgs precision measurements. Note that, if we start from the parameters in the Higgs potential for a specific 2HDM+S model, and impose the theoretical considerations of successful electroweak symmetry breaking, vacuum stability, perturbativity, and unitarity, the resulting values of the mixing angles and mass differences might be restricted to a certain range. These ranges would depend on the particular symmetry assumption of the Higgs potential, and could also be relaxed with the variation of other model parameters. In our analyses, we consider a model independent approach and use the various mixing angles and physics Higgs masses as our relevant model parameters for the *STU* study. We let the mixing angles vary over the whole range and the mass difference up to approximately 1 TeV, which allows a straightforward mapping of a particular Higgs potential scenario to the general results of the electroweak precision constraints that we studied herein.

The remainder of this paper is organized as follows. In Section II, we introduce the theoretical framework of the 2HDM+S, as well as five benchmark cases. In Section III, we introduce the electroweak oblique parameters and the contributions from the Higgs sector in the 2HDM+S. In Section IV, we present 95% C.L. *STU* allowed regions in the 2HDM+S parameter spaces of the five benchmark cases. In Section V, we study the cases beyond the alignment limit. In Section VI, we show the complementarity of electroweak precision analyses with Higgs precision measurements. We conclude this paper in Section VII.

II. THEORETICAL FRAMEWORK

The 2HDM+S is the singlet extension of the 2HDM, which has the following scalar contents:

$$\Phi_1 = \begin{pmatrix} \chi_1^+ \\ \frac{\rho_1 + i\eta_1}{\sqrt{2}} \end{pmatrix}, \quad \Phi_2 = \begin{pmatrix} \chi_2^+ \\ \frac{\rho_2 + i\eta_2}{\sqrt{2}} \end{pmatrix}, \quad S = \frac{\rho_S + i\eta_S}{\sqrt{2}}, \quad (1)$$

where Φ_1 and Φ_2 are the $SU(2)_L$ doublets with hypercharge $Y = 1/2$, and S is the gauge singlet. The general Higgs potential of the 2HDM+S has been introduced in [14], whereas the simplified version of the 2HDM+S potential can be found in [15] when certain symmetries are imposed. After electroweak symmetry breaking, the neutral components of Φ_1, Φ_2, and S develop non-zero vacuum expectation values, v_1, v_2, and v_S, with $\sqrt{v_1^2 + v_2^2} = v \approx 246$ GeV. We also introduce $\tan\beta = \frac{v_2}{v_1}$ with $\beta \in (0, \pi/2)$. Assuming no CP-violation, the mass spectrum of the 2HDM+S includes three neutral CP-even scalars, two neutral CP-odd scalars, and one pair of charged Higgs bosons.

The neutral CP-even states, $\rho_{1,2,S}$ mix together to form three mass eigenstates: the non-SM-like H, the SM-like Higgs h, and the singlet-like h_S, with the 3×3 rota-

tion matrix R

$$\begin{pmatrix} H \\ h \\ h_S \end{pmatrix} = R \begin{pmatrix} \rho_1 \\ \rho_2 \\ \rho_S \end{pmatrix}, \quad R M_S^2 R^T = \mathrm{diag}\{m_H^2, m_h^2, m_{h_S}^2\}. \tag{2}$$

The R matrix is parameterized using three mixing angles α, α_{HS}, and α_{hS}, which characterize the mixing angle between the two neutral components of the Higgs doublets $\rho_{1,2}$, and the mixing angles between the singlet ρ_S with the 2HDM CP-even Higgses:

$$\begin{aligned} R &= \begin{pmatrix} 1 & 0 & 0 \\ 0 & c_{\alpha_{hS}} & s_{\alpha_{hS}} \\ 0 & -s_{\alpha_{hS}} & c_{\alpha_{hS}} \end{pmatrix} \begin{pmatrix} c_{\alpha_{HS}} & 0 & s_{\alpha_{HS}} \\ 0 & 1 & 0 \\ -s_{\alpha_{HS}} & 0 & c_{\alpha_{HS}} \end{pmatrix} \begin{pmatrix} c_\alpha & s_\alpha & 0 \\ -s_\alpha & c_\alpha & 0 \\ 0 & 0 & 1 \end{pmatrix} \\ &= \begin{pmatrix} c_\alpha c_{\alpha_{HS}} & s_\alpha c_{\alpha_{HS}} & s_{\alpha_{HS}} \\ -s_\alpha c_{\alpha_{hS}} - c_\alpha s_{\alpha_{HS}} s_{\alpha_{hS}} & c_\alpha c_{\alpha_{hS}} - s_\alpha s_{\alpha_{HS}} s_{\alpha_{hS}} & c_{\alpha_{HS}} s_{\alpha_{hS}} \\ s_\alpha s_{\alpha_{hS}} - c_\alpha s_{\alpha_{HS}} c_{\alpha_{hS}} & -s_\alpha s_{\alpha_{HS}} c_{\alpha_{hS}} - c_\alpha s_{\alpha_{hS}} & c_{\alpha_{HS}} c_{\alpha_{hS}} \end{pmatrix}, \end{aligned} \tag{3}$$

where we use the shorthand notations $s_x = \sin x$ and $c_x = \cos x$. For the CP-odd states, we have

$$\begin{pmatrix} G^0 \\ A \\ A_S \end{pmatrix} = \begin{pmatrix} 1 & 0 & 0 \\ 0 & & \\ 0 & & R^A \end{pmatrix} \begin{pmatrix} c_\beta & s_\beta & 0 \\ -s_\beta & c_\beta & 0 \\ 0 & 0 & 1 \end{pmatrix} \begin{pmatrix} \eta_1 \\ \eta_2 \\ \eta_S \end{pmatrix},$$
$$R^A = \begin{pmatrix} c_{\alpha_{AS}} & s_{\alpha_{AS}} \\ -s_{\alpha_{AS}} & c_{\alpha_{AS}} \end{pmatrix}, \tag{4}$$

where G^0 is the neutral Goldstone boson, and the angle α_{AS} is the mixing between the 2HDM pseudoscalar and the singlet pseudoscalar η_S. In addition, the charged sector of the 2HDM+S is the same as that of the 2HDM, containing one pair of charged Higgses $H^\pm$ and the Goldstone bosons $G^\pm$. Each of the mixing angles α, α_{HS}, α_{hS}, α_{AS} varies in the range of

$$-\frac{\pi}{2} < \alpha_i < \frac{\pi}{2}. \tag{5}$$

When $\alpha_i = \pm\pi/4$, the mixing between the two Higgs bosons reaches maximum, and the properties of the two corresponding scalars flip when $\pi/4 < |\alpha_i| < \pi/2$. Note that the effects of different signs of the mixing angles appear only when all four mixing angles are nonzero. When at least one mixing angle is nonzero, the properties of the Higgs bosons are independent of the sign of the mixing angles. When the theoretical considerations of successful electroweak symmetry breaking, vacuum stability, perturbativity, and unitarity are imposed on the Higgs potential, the resulting values of the mixing angles might be restricted to a smaller range. These ranges would depend on the particular symmetry assumption of the Higgs potential. We consider the whole range of these mixing angles, which allows a straightforward mapping of a particular Higgs potential scenario to the general results of the electroweak precision constraints that we investigate in this study.

After the diagonalization of the Higgs mass matrices, there are 11 free parameters for the mass eigenstates: six Higgs boson masses, $\tan\beta$, and four mixing angles. As only the couplings between the Higgses and the SM gauge bosons enter the oblique parameters, we focus on the following nine free parameters for our study of the oblique parameters:

$$\underbrace{m_h = 125\ \mathrm{GeV},\ m_H,\ m_A,\ m_{H^\pm},\ \cos(\beta-\alpha)}_{\text{2HDM parameters}},\ \underbrace{m_{h_S},\ m_{A_S},\ \alpha_{HS},\ \alpha_{hS},\ \alpha_{AS}}_{\text{singlet parameters}}. \tag{6}$$

Using the mixing matrices, one can obtain the couplings of physical Higgses to the gauge bosons, which are denoted by the following effective couplings:

$$g^{\mu\nu}_{h_i VV} = c_{h_i VV} \mathrm{i} \frac{2m_V^2}{v} g^{\mu\nu}, \tag{7}$$

where h_i represents all possible neutral CP-even states, including h, H, and h_S, and $V = W, Z$. The normalized couplings $c_{h_i VV}$ are shown in Table 2.

In addition, the gauge boson can couple to two different Higgs bosons: the Z boson couples to two Higgs bosons with different CP properties, and the W bosons couple to neutral and charged Higgs bosons. These interactions can be parameterized as

$$g^{\mu}_{\phi_i\varphi_j V} = c_{\phi_i\varphi_j V}\,\mathrm{i}\frac{m_V}{v}(p^{\mu}_{\phi_i} - p^{\mu}_{\varphi_j}), \tag{8}$$

$$g^{\mu}_{H^-H^+\gamma} = c_{H^+H^-\gamma}\,\mathrm{i}e(p^{\mu}_{H^-} - p^{\mu}_{H^+}), \tag{9}$$

$$g^{\mu}_{H^-H^+Z} = c_{H^+H^-Z}\,\mathrm{i}e\frac{c_W^2 - s_W^2}{s_W c_W}(p^{\mu}_{H^-} - p^{\mu}_{H^+}), \tag{10}$$

where ϕ_i and φ_j correspond to different types of Higgs bosons: φ includes neutral states, and ϕ includes charged Higgs $H^{\pm}$ [1]. Furthermore, the Higgs bosons can couple to gauge bosons via the quartic interactions, which are

$$g^{\mu\nu}_{\varphi_i\varphi_j VV} = c_{\varphi_i\varphi_j VV}\frac{\mathrm{i}2m_V^2}{v^2}g^{\mu\nu}. \tag{11}$$

Given the complexity of the 2HDM+S scalar sectors and the appearance of multiple mixing angles, we consider five benchmark cases to disentangle the impact of each mixing angle. For Case-0, we have all the mixing angles set to be 0, which is the 2HDM alignment limit case. For other cases, only one mixing angle is nonzero, whereas the others are fixed to 0, as shown in Table 1.

- Case-0 with $c_{\beta-\alpha} = \alpha_{HS} = \alpha_{hS} = \alpha_{AS} = 0$ is the 2HDM alignment limit, where the singlet components are decoupled, and the 125 GeV Higgs h is the same as the SM Higgs. In this case, all the couplings of the singlet Higgs bosons h_S, A_S to SM particles are zero, and the beyond the SM (BSM) Higgs coupling HVV is zero. However, the BSM Higgs bosons can still couple to gauge bosons via AHZ, $HH^{\pm}W^{\mp}$, $AH^{\pm}W^{\mp}$, $HHVV$, $AAVV$, and H^+H^-VV couplings.

- Case-I with $\alpha_{HS} = \alpha_{hS} = \alpha_{AS} = 0$ is the 2HDM limit, when the singlet components are completely decoupled. The mixing between H and h is parameterized by α, as in the usual 2HDM.

- Case-II with $\alpha_{hS} \neq 0$ represents the case when the 125 GeV h mixes with the singlet Higgs h_S; thus, the SM-like Higgs properties are similar to those of the singlet extended SM (SSM). However, the BSM doublet components H/A are the same as the alignment limit of the 2HDM.

- Case-III with $\alpha_{HS} \neq 0$ represents the case when the non-SM H mixes with the singlet Higgs h_S, whereas the 125 GeV Higgs h is completely SM-like.

Table 1. Five benchmark cases for the mixing angle configurations

Benchmark Case		Fixed mixing angles	Variable mixing angles
Case-0	(2HDM alignment limit)	$c_{\beta-\alpha} = \alpha_{HS} = \alpha_{hS} = \alpha_{AS} = 0$	—
Case-I	(2HDM limit)	$\alpha_{HS} = \alpha_{hS} = \alpha_{AS} = 0$	$c_{\beta-\alpha}$
Case-II	(SSM limit)	$c_{\beta-\alpha} = \alpha_{HS} = \alpha_{AS} = 0$	α_{hS}
Case-III		$c_{\beta-\alpha} = \alpha_{hS} = \alpha_{AS} = 0$	α_{HS}
Case-IV		$c_{\beta-\alpha} = \alpha_{hS} = \alpha_{HS} = 0$	α_{AS}

- Case-IV with $\alpha_{AS} \neq 0$ represents the case when A mixes with the singlet pseudoscalar A_S, where the CP-even sector is the same as the alignment limit of the 2HDM, plus a decoupled singlet scalar S.

In Table 2, we list the couplings between the Higgses and the SM gauge bosons, which are relevant for the calculation of the oblique parameters. The general expressions are given in the second column, as well as the couplings in the individual Case-0 − Case-IV. As the STU parameters only depend on couplings between the Higgses and gauge bosons, the fermionic couplings of the Higgs bosons are irrelevant in this study. Therefore, the contributions to the STU parameters are independent of the specific structure of the Yukawa couplings. In particular, when the singlet CP-odd Higgs is decoupled by $\alpha_{AS} = 0$, the 2HDM+S is similar to the N2HDM (the real singlet extension of the 2HDM [11]). Note that the $A_S hZ$ and $A_S h_S Z$ couplings are always zero for these benchmark cases, as multiple non-zero mixing angles are needed to couple the CP-odd singlet Higgs A_S to the CP-even Higgs h and h_S. In addition, the quartic coupling $HhVV$ is zero for the benchmark cases and is non-zero only when α_{HS} and α_{hS} are both non-zero.

III. OBLIQUE PARAMETERS

As the oblique parameters STU are constructed with the W and Z self-energies [21], as shown in Eqs. (A2)–(A3), they receive contributions from the Feynman diagrams in Fig. 1. The three-point vertices (including h_iVV, h_ia_jZ, $h_i/a_iH^{\pm}W^{\mp}$, and $Z/\gamma H^{\pm}H^{\mp}$), as well as the four-point vertices (including h_ih_iVV, a_ia_iVV, and $H^{\pm}H^{\mp}VV$), contribute to the self-energies of the gauge bosons.

The contributions to the STU parameters from various Higgses can be found in Ref. [22]. Using those expressions, the STU parameters in the 2HDM+S are given by

1) The notation of ϕ_i represents all possible neutral Higgs bosons, including h, H, h_S, A, and A_S. The notation of φ_j represents all possible Higgs bosons, including h, H, h_S, A, A_S, and $H^{\pm}$. The general expression of $\phi_i\varphi_j V$ couplings includes the couplings of a_ih_jZ, $a_iH^{\pm}W^{\mp}$, and $h_iH^{\pm}W^{\mp}$, where a_i represents A and A_S, and h_j represents h, H, and h_S.

Table 2. Couplings between Higgs bosons and gauge bosons in the 2HDM+S.

	Couplings	Case-0	Case-I	Case-II	Case-III	Case-IV
	$c_{h_iVV}=R_{i1}c_\beta+R_{i2}s_\beta$					
c_{HVV}	$c_{\beta-\alpha}c_{\alpha_{HS}}$	0	$c_{\beta-\alpha}$	0	0	0
c_{hVV}	$s_{\beta-\alpha}c_{\alpha_{hS}}-c_{\beta-\alpha}s_{\alpha_{HS}}s_{\alpha_{hS}}$	1	$s_{\beta-\alpha}$	$c_{\alpha_{hS}}$	1	1
c_{h_SVV}	$-s_{\beta-\alpha}s_{\alpha_{hS}}-c_{\beta-\alpha}s_{\alpha_{HS}}c_{\alpha_{hS}}$	0	0	$-s_{\alpha_{hS}}$	0	0
	$c_{a_ih_jZ}=R^A_{i1}R_{j1}+R^A_{i2}R_{j2}$					
c_{AHZ}	$-c_{\alpha_{AS}}c_{\alpha_{HS}}s_{\beta-\alpha}$	−1	$-s_{\beta-\alpha}$	−1	$-c_{\alpha_{HS}}$	$-c_{\alpha_{AS}}$
c_{AhZ}	$c_{\alpha_{AS}}\left(c_{\beta-\alpha}c_{\alpha_{hS}}+s_{\beta-\alpha}s_{\alpha_{HS}}s_{\alpha_{hS}}\right)$	0	$c_{\beta-\alpha}$	0	0	0
c_{Ah_SZ}	$-c_{\alpha_{AS}}\left(c_{\beta-\alpha}s_{\alpha_{hS}}-s_{\beta-\alpha}s_{\alpha_{HS}}c_{\alpha_{hS}}\right)$	0	0	0	$s_{\alpha_{HS}}$	0
c_{A_SHZ}	$s_{\alpha_{AS}}c_{\alpha_{HS}}s_{\beta-\alpha}$	0	0	0	0	$s_{\alpha_{AS}}$
c_{A_ShZ}	$-s_{\alpha_{AS}}\left(c_{\beta-\alpha}c_{\alpha_{hS}}+s_{\beta-\alpha}s_{\alpha_{HS}}s_{\alpha_{hS}}\right)$	0	0	0	0	0
$c_{A_Sh_SZ}$	$s_{\alpha_{AS}}\left(c_{\beta-\alpha}s_{\alpha_{hS}}-s_{\beta-\alpha}s_{\alpha_{HS}}c_{\alpha_{hS}}\right)$	0	0	0	0	0
	$c_{\phi_iH^\pm W^\mp}=R^\phi_{i2}c_\beta-R^\phi_{i1}s_\beta$					
$c_{HH^\pm W^\mp}$	$-\mathrm{i}c_{\alpha_{HS}}s_{\beta-\alpha}$	−i	$-\mathrm{i}s_{\beta-\alpha}$	−i	$-\mathrm{i}c_{\alpha_{HS}}$	−i
$c_{hH^\pm W^\mp}$	$\mathrm{i}\left(c_{\beta-\alpha}c_{\alpha_{hS}}+s_{\beta-\alpha}s_{\alpha_{HS}}s_{\alpha_{hS}}\right)$	0	$\mathrm{i}c_{\beta-\alpha}$	0	0	0
$c_{h_SH^\pm W^\mp}$	$-\mathrm{i}\left(c_{\beta-\alpha}s_{\alpha_{hS}}-s_{\beta-\alpha}s_{\alpha_{HS}}c_{\alpha_{hS}}\right)$	0	0	0	$-\mathrm{i}s_{\alpha_{HS}}$	0
$c_{AH^\pm W^\mp}$	$c_{\alpha_{AS}}$	1	1	1	1	$c_{\alpha_{AS}}$
$c_{A_SH^\pm W^\mp}$	$-s_{\alpha_{AS}}$	0	0	0	0	$-s_{\alpha_{AS}}$
	$c_{\phi_i\phi_jVV}=R^\phi_{i1}R^\phi_{j1}+R^\phi_{i2}R^\phi_{j2}$					
c_{HHVV}	$c^2_{\alpha_{HS}}$	1	1	1	$c^2_{\alpha_{HS}}$	1
c_{hhVV}	$c^2_{\alpha_{hS}}+s^2_{\alpha_{HS}}s^2_{\alpha_{hS}}$	1	1	$c^2_{\alpha_{hS}}$	1	1
$c_{h_Sh_SVV}$	$c^2_{\alpha_{hS}}s^2_{\alpha_{HS}}+s^2_{\alpha_{hS}}$	0	0	$s^2_{\alpha_{hS}}$	$s^2_{\alpha_{HS}}$	0
c_{HhVV}	$-\frac{1}{2}s_{2\alpha_{HS}}s_{\alpha_{hS}}$	0	0	0	0	0
c_{Hh_SVV}	$-\frac{1}{2}s_{2\alpha_{HS}}c_{\alpha_{hS}}$	0	0	0	$-\frac{1}{2}s_{2\alpha_{HS}}$	0
c_{hh_SVV}	$-\frac{1}{2}c^2_{\alpha_{HS}}s_{2\alpha_{hS}}$	0	0	$-\frac{1}{2}s_{2\alpha_{hS}}$	0	0
c_{AAVV}	$c^2_{\alpha_{AS}}$	1	1	1	1	$c^2_{\alpha_{AS}}$
$c_{A_SA_SVV}$	$s^2_{\alpha_{AS}}$	0	0	0	0	$s^2_{\alpha_{AS}}$
c_{AA_SVV}	$-\frac{1}{2}s_{2\alpha_{AS}}$	0	0	0	0	$-\frac{1}{2}s_{2\alpha_{AS}}$
$c_{H^\pm H^\mp Z}$		1	1	1	1	1
$c_{H^\pm H^\mp\gamma}$		1	1	1	1	1
$c_{H^\pm H^\mp VV}$		1	1	1	1	1
Relevant mixing		—	H,h	h,h_S	H,h_S	A,A_S

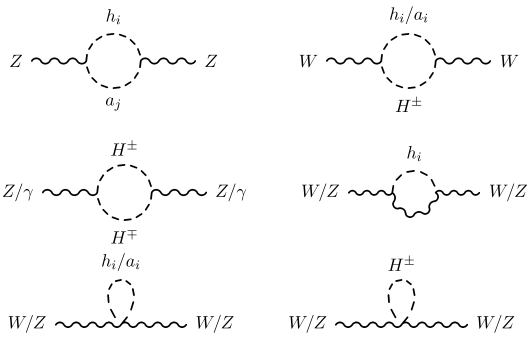

Fig. 1. Feynman diagrams that contribute to the self energy of the SM gauge bosons.

$$S = \frac{1}{24\pi}\Bigg[(2s_W^2-1)^2 G(m_{H^\pm}^2, m_{H^\pm}^2, m_Z^2) + \sum_{i,j}|c_{a_i h_j Z}|^2 G(m_{a_i}^2, m_{h_j}^2, m_Z^2) + \sum_{i=1}^{3} c_{h_i h_i VV}\ln(m_{h_i}^2)$$
$$+ \sum_{i=1}^{2} c_{a_i a_i VV}\ln(m_{a_i}^2) - 2\ln(m_{H^\pm}^2) - \ln(m_{h_{\rm ref}}^2) + \sum_{i=1}^{3}|c_{h_i VV}|^2 \hat{G}(m_{h_i}^2, m_Z^2) - \hat{G}(m_{h_{\rm ref}}^2, m_Z^2)\Bigg], \tag{12}$$

$$T = \frac{1}{16\pi s_W^2 m_W^2}\Bigg[\sum_{i=1}^{3}|c_{h_i H^\pm W^\mp}|^2 F(m_{H^\pm}^2, m_{h_i}^2) + \sum_{i=1}^{2}|c_{a_i H^\pm W^\mp}|^2 F(m_{H^\pm}^2, m_{a_i}^2) - \sum_{i,j}|c_{a_i h_j Z}|^2 F(m_{a_i}^2, m_{h_j}^2)$$
$$+ 3\sum_{i=1}^{3}|c_{h_i VV}|^2\left(F(m_Z^2, m_{h_i}^2) - F(m_W^2, m_{h_i}^2)\right) - 3\left(F(m_Z^2, m_{h_{\rm ref}}^2) - F(m_W^2, m_{h_{\rm ref}}^2)\right)\Bigg], \tag{13}$$

$$U = \frac{1}{24\pi}\Bigg[\sum_{i=1}^{3}|c_{h_i H^\pm W^\mp}|^2 G(m_{H^\pm}^2, m_{h_i}^2, m_W^2) + \sum_{i=1}^{2}|c_{a_i H^\pm W^\mp}|^2 G(m_{H^\pm}^2, m_{a_i}^2, m_W^2) - (2s_W^2-1)^2 G(m_{H^\pm}^2, m_{H^\pm}^2, m_Z^2)$$
$$- \sum_{i,j}|c_{a_i h_j Z}|^2 G(m_{a_i}^2, m_{h_j}^2, m_Z^2) + \sum_{i=1}^{3}|c_{h_i VV}|^2\left(\hat{G}(m_{h_i}^2, m_W^2) - \hat{G}(m_{h_i}^2, m_Z^2)\right) - \hat{G}(m_{h_{\rm ref}}^2, m_W^2) + \hat{G}(m_{h_{\rm ref}}^2, m_Z^2)\Bigg], \tag{14}$$

where $m_{h_{\rm ref}} = 125$ GeV is the reference mass of the SM Higgs. The functions F, G, and $\hat{G}$ can be found in Eqs. (A4), (A5), and (A6) in Appendix A.

For the T parameter, the contributions from the quartic couplings are canceled out, as $\varphi_i\varphi_i WW$ are the same as $\varphi_i\varphi_i ZZ$ and the T observable is defined by the self-energy difference between the W boson and Z boson (see Eq. (A1)). Thus, the T observable only receives the contribution from the $h_i VV$, $a_i h_j Z$, and $a_i/h_i H^\pm W^\mp$ couplings. Furthermore, the S parameter mainly represents the Z boson self-energy, and receives contributions from the $ZH^\pm H^\mp$ interaction via $G(m_{H^\pm}^2, m_{H^\pm}^2, m_Z^2)$ and the $a_i h_j Z$ interaction via $G(m_{a_i}^2, m_{h_j}^2, m_Z^2)$. In addition, the quartic couplings $h_i h_i VV$, $a_i a_i VV$, and $H^\pm H^\pm VV$ enter into the S parameter via the logarithmic functions. For the U parameter, the contributions of the quartic interactions are canceled out again. Furthermore, the U parameter is related to the dim-8 operator, which is usually suppressed. Therefore, in our discussion below, we mostly focus on the S and T parameters, which are more sensitive to the BSM effects.

The experimental measurements for the electroweak precision observables yield the following best-fit values of STU [28] for $m_{h_{\rm ref}} = 125$ GeV:

$$\begin{aligned} S^{\rm exp} &= -0.04, & T^{\rm exp} &= 0.01, & U^{\rm exp} &= -0.01, \\ \Delta S &= 0.10, & \Delta T &= 0.12, & \Delta U &= 0.09, \\ {\rm corr}(S,T) &= +0.93, & {\rm corr}(S,U) &= -0.70, & {\rm corr}(T,U) &= -0.87, \end{aligned} \tag{15}$$

where ${\rm corr}(S,T)$, ${\rm corr}(S,U)$, and ${\rm corr}(T,U)$ are the correlation coefficients between S, T, and U. The contributions to the oblique parameters STU in the 2HDM+S, *i.e.*, Eqs. (13), (12), and (14), can be used to obtain the χ^2 value [26, 29],

$$\chi^2_{STU} = \left(S - S^{\rm exp}, \quad T - T^{\rm exp}, \quad U - U^{\rm exp}\right)\cdot \mathbf{cov}^{-1}\cdot \begin{pmatrix} S - S^{\rm exp} \\ T - T^{\rm exp} \\ U - U^{\rm exp} \end{pmatrix}, \tag{16}$$

where

$$\mathbf{cov} = \begin{pmatrix} \Delta S^2 & {\rm corr}(S,T)\Delta S\Delta T & {\rm corr}(S,U)\Delta S\Delta U \\ {\rm corr}(S,T)\Delta S\Delta T & \Delta T^2 & {\rm corr}(T,U)\Delta T\Delta U \\ {\rm corr}(S,U)\Delta S\Delta U & {\rm corr}(T,U)\Delta T\Delta U & \Delta U^2 \end{pmatrix}. \tag{17}$$

The two-dimensional fit to the STU parameters at 95% C.L. corresponds to $\Delta\chi^2 = \chi^2_{STU} - \chi^2_{STU}|_{\rm minimal} < 5.99$.

IV. FIVE BENCHMARK CASES

In the 2HDM, the *STU* parameters play an important role in constraining the mass splittings between the BSM neutral Higgses and the charged Higgses $H^\pm$. In the 2HDM+S, the singlet field enters via the mixing, which further changes the dependence of the *STU* parameters on the model parameters. In this section, we explore the impacts of electroweak constraints on the mixing angles, $\beta-\alpha$, α_{hS}, α_{HS}, and α_{AS}, as well as various mass splittings. For convenience, we define the following mass splittings, which are relevant for the *STU* constraints:

$$\Delta m_H = m_H - m_{H^\pm}, \quad \Delta m_A = m_A - m_{H^\pm},$$
$$\Delta m_{h_S} = m_{h_S} - m_{H^\pm}, \quad \Delta m_{A_S} = m_{A_S} - m_{H^\pm}. \tag{18}$$

With a general scan of the model parameters in the Higgs potential with theoretical considerations taken into account, we find that a relatively large range of mass differences is allowed, particularly with the variation of the soft Z_2 breaking mass parameter in the Higgs potential.

A. Case-0

For a starting point, we study the simplest Case-0 (the 2HDM alignment limit) with $c_{\beta-\alpha} = \alpha_{HS} = \alpha_{hS} = \alpha_{AS} = 0$. According to Table 2, the non-zero couplings in this case are

$$c_{hVV},\ c_{AHZ},\ c_{HH^\pm W^\mp},\ c_{AH^\pm W^\mp},\ c_{ZH^\pm H^\mp},$$
$$c_{hhVV},\ c_{HHVV},\ c_{AAVV},\ c_{H^\pm H^\pm VV}, \tag{19}$$

with norm 1. The 125 GeV Higgs h is the SM Higgs, and singlet Higgs bosons h_S and A_S both decouple. The doublet BSM Higgses H, A, and $H^\pm$ enter via AHZ, $HH^\pm W^\mp$, and $AH^\pm W^\mp$ interactions and mainly contribute to the terms involving F functions in the T parameter. In addition, $ZH^\pm H^\mp$ and quartic interactions $HHVV$, $AAVV$, and $H^\pm H^\mp VV$ contribute to the S parameter. Consequently, the masses of H, A, and $H^\pm$ are relevant for the oblique parameters, whereas the singlet Higgs masses m_{h_S} and m_{A_S} are irrelevant.

The T and S parameters in this case, denoted as T_0 and S_0, respectively, are given by [29]

$$T_0 = \frac{1}{16\pi s_W^2 m_W^2}[F(m_{H^\pm}^2, m_H^2) - F(m_A^2, m_H^2) + F(m_{H^\pm}^2, m_A^2)], \tag{20}$$

$$S_0 = \frac{1}{24\pi}[(2s_W^2-1)^2 G(m_{H^\pm}^2, m_{H^\pm}^2, m_Z^2) + G(m_A^2, m_H^2, m_Z^2) + \ln\left(\frac{m_H^2}{m_{H^\pm}^2}\right) + \ln\left(\frac{m_A^2}{m_{H^\pm}^2}\right)], \tag{21}$$

The values of T_0 with varying Δm_H and Δm_A are presented by the solid lines in Fig. 2. The left panel indicates varying Δm_H with fixed $\Delta m_A = 0$, ± 50 GeV, and the right panel indicates varying Δm_A with fixed $\Delta m_H = 0$, ± 50 GeV. As indicated by Eq. (20), T_0 is exactly zero when $\Delta m_H = 0$ or $\Delta m_A = 0$. The grey hatch area is the 1σ region of the electroweak precision observable fit to the T parameter. T_0 is also symmetric under the exchange of m_H and m_A. Therefore, the T_0 dependence on Δm_H in the left panel is the same as the T_0 dependence on Δm_A in the right panel. T_0 increases as Δm_H (Δm_A) increases for $\Delta m_A > 0$ ($\Delta m_H > 0$) but decreases for the opposite sign of Δm_A (Δm_H). Furthermore, $T_0 > 0$ when both Δm_H and Δm_A have the same sign, and $T_0 < 0$ when Δm_H and Δm_A

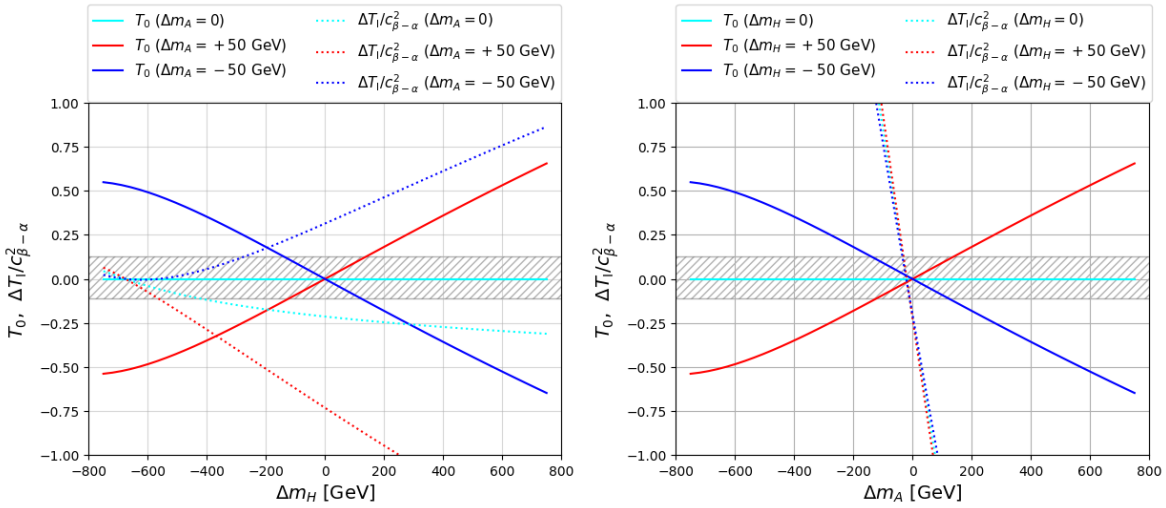

Fig. 2. (color online) T_0 (solid lines) and $\Delta T_1/c^2_{\beta-\alpha}$ (dotted lines) with varying Δm_H (left) and Δm_A (right). The cyan, red, and blue lines indicate $\Delta m_{A,H}$ =0, + 50 GeV, and −50 GeV, respectively. The grey hatch area is the 1σ region of the T observable. $m_{H^\pm}$ is chosen to be 800 GeV.

have opposite signs.

However, the S_0 parameter is not zero even when both Δm_A and Δm_H are zero. The contributions from $G(m_i^2, m_j^2, m_k^2)$ are typically very small. The main contributions to S_0 come from the logarithmic terms $\ln(m_{H,A}^2/m_{H^\pm}^2)$. For $\Delta m_{H,A}$ in the range of ± 700 GeV, $|S_0| < 0.15$ is within the 1 σ range of the fitted value.

Figure 3 shows the 95% C.L. allowed region from the *STU* constraints in the Δm_H vs. Δm_A plane. The blue region corresponds to Case-0 with $c_{\beta-\alpha} = \alpha_{HS} = \alpha_{hS} = \alpha_{AS} = 0$ and $m_{H^\pm} = 800$ GeV, which centers around $\Delta m_H = 0$ or $\Delta m_A = 0$. Owing to the positive correlation between the S and T observables, the area with positive T is preferred. Therefore, the allowed regions with the same signs of Δm_A and Δm_H are larger than the allowed regions with opposite signs.

In Fig. 4, the 95% C.L. allowed regions under the *STU* constraints are shown in the $\Delta m_{A,H}$ vs. $c_{\beta-\alpha}$ plane. For $c_{\beta-\alpha} = 0$, the 95% C.L. fit to the *STU* parameters gives $\Delta m_{A,H} \lesssim 900$ GeV with $\Delta m_{H,A} = 0$ for $m_{H^\pm} = 800$ GeV (blue region). The upper limits on $\Delta m_{A,H}$ come from the logarithm contributions. Note that a large mass difference can be allowed after theoretical considerations are taken into account, as long as m_{12} and other model parameters are allowed to vary within a certain range. These upper limits of $\Delta m_{A,H}$ vary with the benchmark value of $m_{H^\pm}$ and increase as $H^\pm$ becomes heavier, as indicated by the green dashed curve for $m_{H^\pm} = 1000$ GeV. For non-zero values of $\Delta m_{A,H} = \pm 50$ GeV, the allowed range of $\Delta m_{H,A}$ is much smaller, as shown by the regions with the

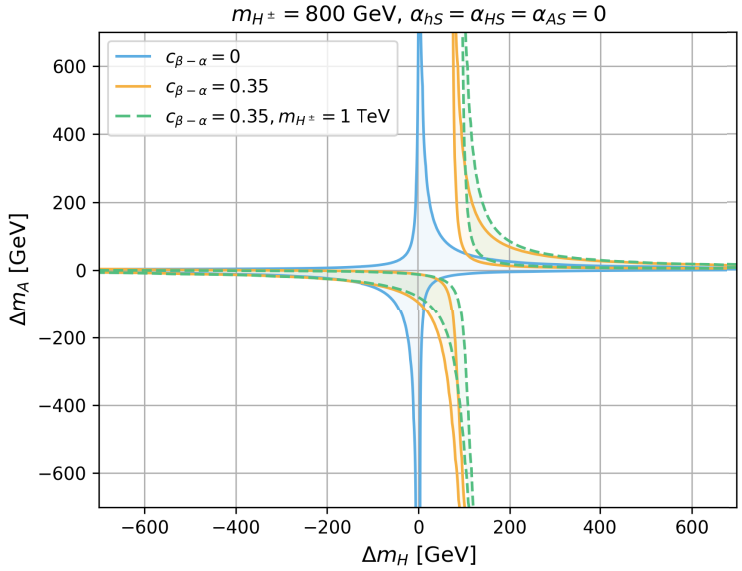

Fig. 3. (color online) 95% C.L. allowed region from *STU* constraints in the plane Δm_H vs. Δm_A with $c_{\beta-\alpha} = 0$ (solid blue region) and 0.35 (solid orange region) for $m_{H^\pm} = 800$ GeV. The other parameters are $\alpha_{HS} = \alpha_{hS} = \alpha_{AS} = 0$. For $m_{H^\pm} = 1000$ GeV, the allowed region for $c_{\beta-\alpha} = 0$ is approximately the same as that for $m_{H^\pm} = 800$ GeV, whereas the region for $c_{\beta-\alpha} = 0.35$ is shown by the green regions.

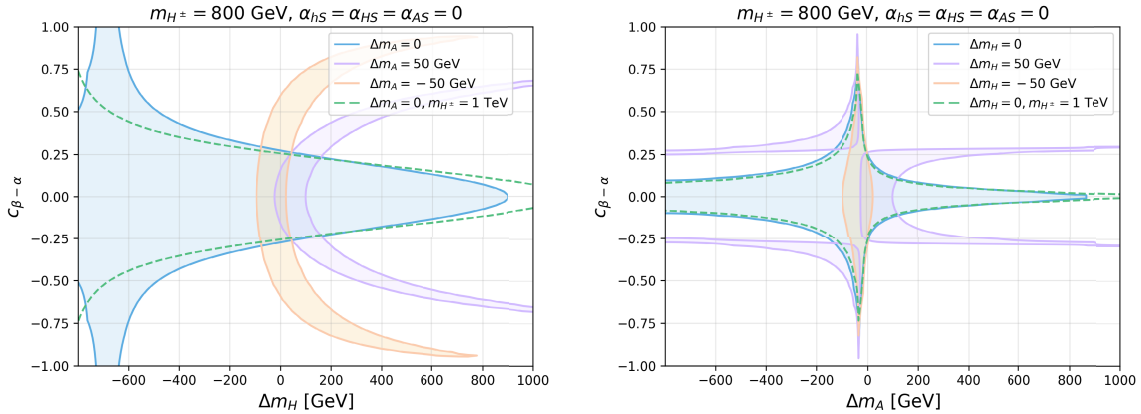

Fig. 4. (color online) 95% C.L. allowed region via *STU* constraints on $c_{\beta-\alpha}$ vs. Δm_H (left) and Δm_A vs. $c_{\beta-\alpha}$ (right). The other parameters are chosen as $\alpha_{HS} = \alpha_{hS} = \alpha_{AS} = 0$ and $m_H^\pm = 800$ GeV (solid curves). The blue, purple, and orange regions correspond to $\Delta m_{A,H} = 0$, 50, -50 GeV, respectively. The green dashed curves represent $m_{H^\pm} = 1000$ GeV and $\Delta m_{A,H=0}$.

purple and orange boundary curves in Fig. 4.

B. Case-I: $c_{\beta-\alpha} \neq 0$

In Case-I ($c_{\beta-\alpha} \neq 0$ and $\alpha_{HS} = \alpha_{hS} = \alpha_{AS} = 0$), the singlet fields decouple completely, and the model is the same as the 2HDM. In particular, we have the following non-zero couplings in addition to those shown in Eq. (19)

$$c_{HVV}, \quad c_{AhZ}, \quad c_{hH^\pm W^\mp}, \tag{22}$$

which are proportional to $c_{\beta-\alpha}$ and provide additional contributions to the *STU* parameters. Similar to Case-0, the singlet masses m_{h_S} and m_{A_S} are irrelevant, and only the doublet-like Higgs masses m_H, m_A, and $m_{H^\pm}$ enter. The *STU* constraints of the 2HDM have been studied in the literature [26, 30]. The T observable in Case-I is

$$T_{\rm I} = T_0 + \Delta T_{\rm I}, \tag{23}$$

$$\begin{aligned}\Delta T_{\rm I} = \frac{c^2_{\beta-\alpha}}{16\pi s^2_W m^2_W}\{&F(m^2_h, m^2_{H^\pm}) - F(m^2_h, m^2_A)\\ &-[F(m^2_H, m^2_{H^\pm}) - F(m^2_H, m^2_A)]\\ &-3[F(m^2_h, m^2_Z) - F(m^2_h, m^2_{W^\pm})]\\ &+3[F(m^2_H, m^2_Z) - F(m^2_H, m^2_{W^\pm})]\}.\end{aligned} \tag{24}$$

Compared with Case-0, the additional contribution of $\Delta T_{\rm I}$ is proportional to $c_{\beta-\alpha}$, which is non-zero even for $\Delta m_A = 0$.

In Fig. 2, we show the values of T_0 (solid curves) and $\Delta T_{\rm I}/c^2_{\beta-\alpha}$ (dashed curves) for different values of Δm_H and Δm_A. The left panel shows that, for $\Delta m_H = -675$ GeV, which corresponds to $m_H = m_h = 125$ GeV, $\Delta T_{\rm I} = 0$. The right panel shows that $\Delta T_{\rm I}$ has the opposite (same) sign of T_0 for positive (negative) Δm_H, except for a small negative Δm_A region.

The 95% C.L. *STU* allowed parameter space in the Δm_H vs. Δm_A plane is shown in Fig. 3 for $c_{\beta-\alpha} = 0.35$ (orange). The allowed regions shift to the right ($\Delta m_H > 0$), given the cancellation between T_0 and $\Delta T_{\rm I}$. In particular, the $\Delta m_A = 0$ point with $\Delta m_H \sim 100$ GeV and $c_{\beta-\alpha} = 0.35$ would be excluded, as T_0 is zero and cannot eliminate the non-zero $\Delta T_{\rm I}$. The regions enclosed by the green dashed curves indicate $m_{H^\pm} = 1000$ GeV, which is close to the orange regions of $m_{H^\pm} = 800$ GeV.

The left panel of Fig. 4 shows the 95% C.L. *STU* allowed parameter space in $c_{\beta-\alpha}$ vs. Δm_H for various Δm_A. The allowed regions are symmetric with respect to $c_{\beta-\alpha} = 0$, given the $c^2_{\beta-\alpha}$ dependence. For $\Delta m_A = 0$ (region enclosed by the solid blue curve), all the values of $c_{\beta-\alpha}$ are allowed at $m_H = 125$ GeV: $T_0 = 0$ since $\Delta m_A = 0$, and $\Delta T_{\rm I} = 0$ for $m_H = m_h = 125$ GeV. The allowed regions shrink for larger $|m_H - m_{h_{125}}|$. The green dashed line indicates the impact of the value of $m^\pm_H$. For non-zero Δm_A, the non-zero T_0 could be cancelled by $\Delta T_{\rm I}$. The allowed regions favor mostly positive Δm_H, as shown by the regions enclosed by the purple curves and orange curves. As the absolute value of $\Delta T_{\rm I}$ is larger when Δm_A is positive as shown in Fig. 2, the allowed regions with positive Δm_A favor smaller $|c_{\beta-\alpha}|$. The 2HDM non-alignment case has been studied in [30], which did not cover the case with much larger mass splittings.

The right panel of Fig. 4 shows the 95% C.L. *STU* allowed parameter space in $c_{\beta-\alpha}$ vs. Δm_A for various Δm_H. For $\Delta m_H = 0$ (region enclosed by the solid blue curves), a relatively large region of $c_{\beta-\alpha}$ is allowed for $\Delta m_A \sim -30$ GeV, when $\Delta T_{\rm I} \sim 0$ and S_0 and T_0 are small. The allowed regions of $c_{\beta-\alpha}$ for $\Delta m_A > 0$ are smaller than those for $\Delta m_A < 0$, as $|\Delta T_{\rm I}|$ is larger for positive Δm_A. Note that, for negative $\Delta m_H = -50$ GeV, only a narrow range of Δm_A around -30 GeV is allowed. This is because $\Delta T_{\rm I}$ has the same signs as T_0 for negative Δm_H. Therefore, only small values of Δm_A are allowed. However, for positive $\Delta m_H = 50$ GeV, $\Delta T_{\rm I}$ and T_0 have opposite signs. A wide range of Δm_A is allowed: $|c_{\beta-\alpha}| \lesssim 0.25$ for $\Delta m_A > 0$, and $|c_{\beta-\alpha}| \gtrsim 0.25$ for $\Delta m_A < 0$.

C. Case-II: $\alpha_{hS} \neq 0$

In Case-II (*e.g.*, $\alpha_{hS} \neq 0$ and $c_{\beta-\alpha} = \alpha_{HS} = \alpha_{AS} = 0$), the 125 GeV Higgs h mixes with the singlet-like Higgs h_S, and the $h_S VV$ coupling is proportional to $s_{\alpha_{hS}}$, which is the only non-zero trilinear coupling between Higgs and gauge bosons, in addition to those in Eq. (19). The $Ah_S Z$ and $h_S H^\pm W^\mp$ couplings are still zero, which indicates that α_{hS} cannot connect the h_S with the BSM doublet-like Higgses H, A, or $H^\pm$. This case is similar to the singlet extension of the SM (SSM), where the singlet Higgs only mixes with the SM Higgs h. Therefore, the *STU* parameters receive additional contribution via loops with $h_S VV$ vertices, with the singlet Higgs mass m_{h_S} entering. The S and T parameters are given by

$$S_{\rm II} = S_0 + \Delta S_{\rm II}, \quad T_{\rm II} = T_0 + \Delta T_{\rm II}, \tag{25}$$

$$\begin{aligned}\Delta S_{\rm II} = \frac{1}{24\pi} s^2_{\alpha_{hS}}\Big[&\ln\left(\frac{m^2_{h_S}}{m^2_{h_{125}}}\right) + \hat{G}(m^2_{h_S}, m^2_Z)\\ &-\hat{G}(m^2_{h_{125}}, m^2_Z)\Big],\end{aligned} \tag{26}$$

$$\begin{aligned}\Delta T_{\rm II} = \frac{1}{16\pi s^2_W m^2_W} 3 s^2_{\alpha_{hS}}\Big[&F(m^2_Z, m^2_{h_S}) - F(m^2_W, m^2_{h_S})\\ &-F(m^2_Z, m^2_{h_{125}}) + F(m^2_W, m^2_{h_{125}})\Big].\end{aligned} \tag{27}$$

The expression for the function $\hat{G}$ can be found in Eq.

(A6). Note that $\Delta T_{\rm II}$ and $\Delta S_{\rm II}$ are proportional to $s^2_{\alpha_{hS}}$, and both terms vanish when $m_{h_S} = m_{h_{125}}$. $\Delta S_{\rm II}$ is, in general, suppressed, whereas $\Delta T_{\rm II}$ could receive a significant contribution when m_{h_S} is away from 125 GeV, which is negative (positive) for $m_{h_S} > (<)$ 125 GeV. Meanwhile, the masses of H, A, or $H^\pm$ can still contribute via T_0 and S_0.

In the left panel of Fig. 5, we show the 95% C.L. allowed region from the *STU* constraints in the m_{h_S} vs. α_{hS} plane for different values of $\Delta m_H = \Delta m_A$. For $\Delta m_H = \Delta m_A = 0$ (blue), all values of α_{hS} are allowed for $m_{h_S} = m_h \approx 125$ GeV. The allowed region for α_{hS} reduces for m_{h_S} away from 125 GeV: $|\alpha_{hS}| \lesssim 0.7$ for light $m_{h_S} = 10$ GeV and $|\alpha_{hS}| \lesssim 0.2$ for $m_{h_S} = 1$ TeV.

For $\Delta m_H = \Delta m_A = 50$ GeV (orange), the 95% C.L. allowed region shifted to the right of $m_{h_S} = 125$ GeV, owing to the opposite signs of T_0 and $\Delta T_{\rm II}$ for $m_{h_S} > 125$ GeV. For $\Delta m_H = \Delta m_A = 100$ GeV (green), T_0 is so large that only two thin branches in $m_{h_S} > 240$ GeV and $0.5 < |\alpha_{hS}| < \pi/2$ are allowed.

In the right panel of Fig. 5, we show the 95% C.L. *STU* allowed region in the m_{h_S} vs. $\Delta m_{H,A}$ plane for $\alpha_{hS} = 0$ (blue), $\pi/4$(orange), and $\pi/2$ (green). For $\alpha_{hS} = 0$, the bound of $|\Delta m_H| = |\Delta m_A| \lesssim 80$ GeV is independent of m_{h_S}. For non-zero α_{hS}, the allowed value in $|\Delta m_{H,A}|$ reduces for $m_{h_S} < 125$ GeV but increases for $m_{h_S} > 125$ GeV. Note that all curves cross at $m_{h_S} = 125$ GeV, as $\Delta T_{\rm II}$ and $\Delta S_{\rm II}$ vanish at $m_{h_S} = 125$ GeV regardless of the value of α_{hS}. There is a slight asymmetry between the positive and negative values of $\Delta m_H = \Delta m_A$. This is because the S_0 observable is not symmetric between positive and negative $\Delta m_{H,A}$. $\Delta S_{\rm II}$ is always positive for $m_{h_S} > m_{h_{125}}$, whereas the sign of S_0 flips for different signs of $\Delta m_{H,A}$. Therefore, the S observable is larger for positive $\Delta m_{H,A}$ and the constraint would be stronger, which leads to the allowed region for $\Delta m_{H,A} > 0$ being slightly smaller than that in the negative mass difference case.

D. Case-III: $\alpha_{HS} \neq 0$

Case-III corresponds to $\alpha_{HS} \neq 0$ and $c_{\beta-\alpha} = \alpha_{hS} = \alpha_{AS} = 0$, when h_S mixes with the doublet-like CP-even Higgs H. The non-zero trilinear Higgs to gauge-boson couplings include

$$c_{Ah_SZ}, \quad c_{h_SH^\pm W^\mp}, \tag{28}$$

in addition to those in Eq. (19). However, the h_SVV coupling remains zero in this case. While the additional contribution to the S observable is small, the T observable could receive significant contributions:

$$\begin{aligned} T = &\frac{1}{16\pi s_W^2 m_W^2}[c^2_{\alpha_{HS}} F(m^2_{H^\pm}, m^2_H) + s^2_{\alpha_{HS}} F(m^2_{H^\pm}, m^2_{h_S})] \\ &+ F(m^2_{H^\pm}, m^2_A) - [c^2_{\alpha_{HS}} F(m^2_A, m^2_H) + s^2_{\alpha_{HS}} F(m^2_A, m^2_{h_S})]. \end{aligned} \tag{29}$$

$$= T_0 + \Delta T_{\rm III}, \tag{30}$$

$$\begin{aligned} \Delta T_{\rm III} = &\frac{s^2_{\alpha_{HS}}}{16\pi s_W^2 m_W^2}[F(m^2_{H^\pm}, m^2_{h_S}) - F(m^2_A, m^2_{h_S}) \\ &- F(m^2_{H^\pm}, m^2_H) + F(m^2_A, m^2_H)]. \end{aligned} \tag{31}$$

In addition to $\Delta m_{H,A}$, $\Delta m_{h_S} = m_{h_S} - m_{H^\pm}$ enters.

There is a numerical approximation for the F function in Eq. (A4):

$$\begin{aligned} &c^2_\alpha[F(J^2, I^2) - F(K^2, I^2)] + s^2_\alpha[F(J^2, L^2) - F(K^2, L^2)] \\ \approx &F(J^2, [c^2_\alpha I + s^2_\alpha L]^2) - F(K^2, [c^2_\alpha I + s^2_\alpha L]^2). \end{aligned} \tag{32}$$

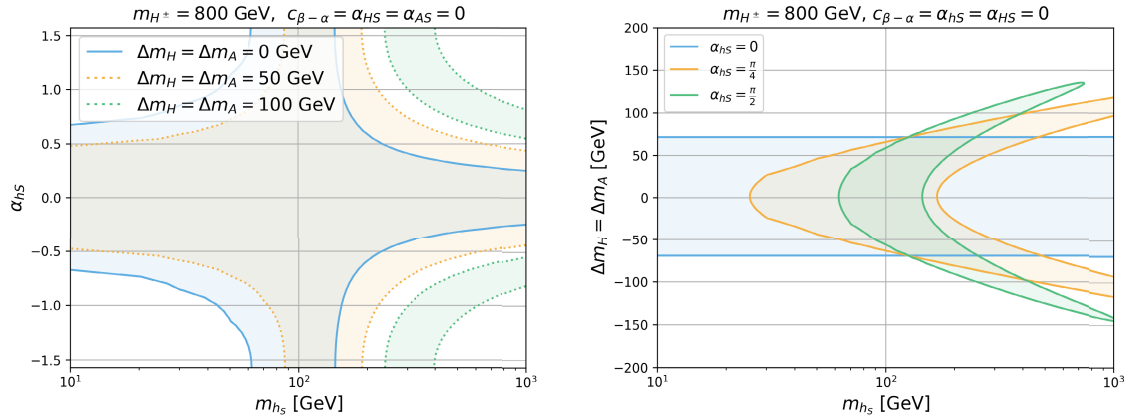

Fig. 5. (color online) 95% C.L. *STU* constraints on the parameter space of m_{h_S}, α_{hS}, and Δm_A. The left panel indicates m_{h_S} vs. α_{hS} with varying Δm_A. The blue, orange, and green regions indicate $\Delta m_A = \Delta m_H = 0$, 50, 100 GeV, respectively. The right panel indicates m_{h_S} vs. $\Delta m_{H,A}$ with varying α_{hS}. The blue, orange, and green regions indicate $\alpha_{hS} = 0$, $\pi/4$, and $\pi/2$, respectively. For both panels, we set $m_{H^\pm} = 800$ GeV and $c_{\beta-\alpha} = \alpha_{HS} = \alpha_{AS} = 0$.

Therefore, the T observable can be approximated as

$$T \approx \frac{1}{16\pi s_W^2 m_W^2}[F(m_{H^\pm}^2,(c_{\alpha_{HS}}^2 m_H + s_{\alpha_{HS}}^2 m_{h_S})^2) - F(m_A^2,(c_{\alpha_{HS}}^2 m_H + s_{\alpha_{HS}}^2 m_{h_S})^2) + F(m_{H^\pm}^2, m_A^2)] \quad (33)$$

which vanishes for

$$c_{\alpha_{HS}}^2 m_H + s_{\alpha_{HS}}^2 m_{h_S} = m_{H^\pm}, \quad \text{or} \quad m_A = m_{H^\pm}. \quad (34)$$

Figure 6 presents the 95% *STU* allowed region in the Δm_H vs. Δm_A plane for Case-III. The region enclosed by the dark blue curves corresponds to the baseline Case-0 when $\alpha_{HS} = 0$. For $\alpha_{HS} = \pi/4$ and $\Delta m_{hS} = 0$ (region enclosed by the light dotted blue lines), the 95% C.L. *STU* allowed region would be slightly enlarged compared with that in Case-0, as the mass-splitting effect of H with $H^\pm$ is suppressed by $c_{\alpha_{HS}}^2 = 1/2$, whereas h_S has no mass splitting with the charged Higgs, as shown in Eq. (34).

When the singlet-like Higgs mass deviates from the charged Higgs mass, for instance, $\Delta m_{hS} = \pm 400$ GeV with $\alpha_{HS} = \pi/4$, as shown by the orange and green regions, the center of the allowed region in Δm_H shifts to the region of $\Delta m_H \approx \mp 400$ GeV to satisfy the mass relation in Eq. (34) to suppress the contributions to the T parameter. Note that $\Delta m_A = 0$ is still allowed, regardless of the choices of Δm_H, Δm_{h_S}, and α_{HS}.

In the left panel of Fig. 7, we show the 95% C.L. *STU* allowed region in the Δm_H vs. Δm_{hS} plane in Case-III for

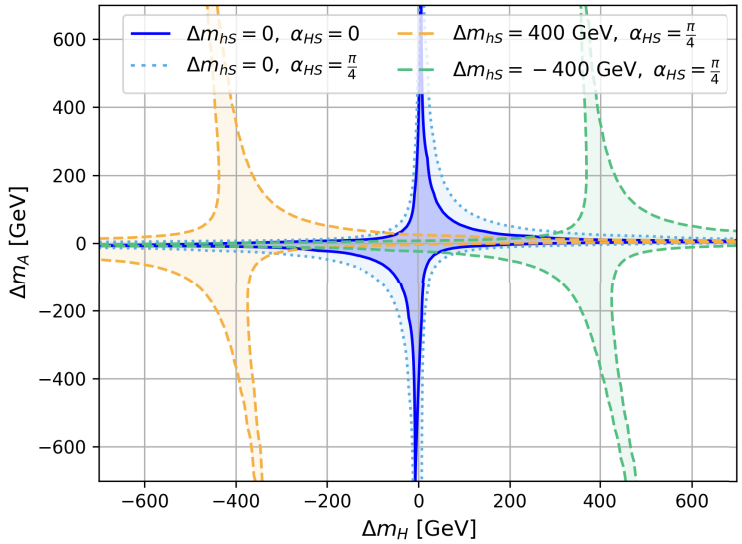

Fig. 6. (color online) 95% C.L. *STU* allowed region in Δm_H vs. Δm_A in Case-III with $c_{\beta-\alpha} = \alpha_{hS} = \alpha_{AS} = 0$. $m_{H^\pm}$ is set to be 800 GeV. The regions enclosed by the dark solid blue and light dashed blue curves indicate $\Delta m_{hS} = 0$ and $\alpha_{HS} = 0$ and $\pi/4$, respectively. The orange and green regions indicate $\Delta m_{hS} = \pm$ 400 GeV, respectively, and $\alpha_{HS} = \pi/4$.

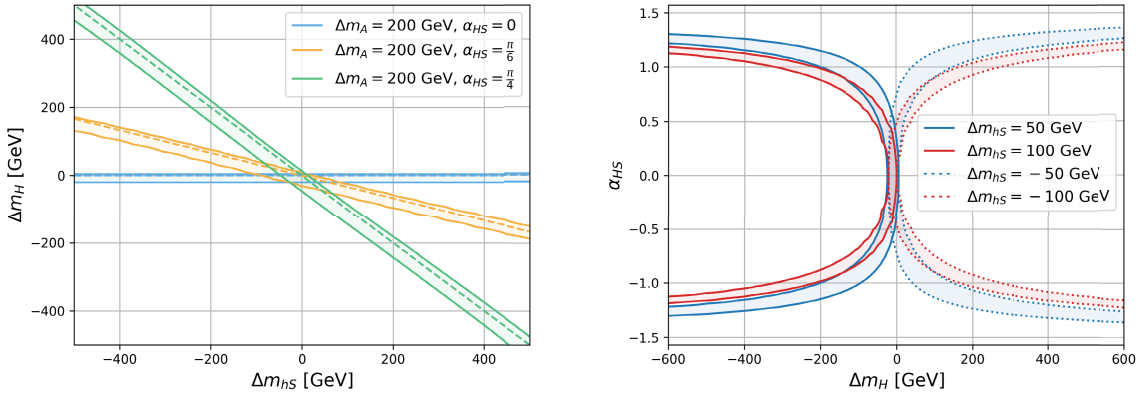

Fig. 7. (color online) 95% C.L. *STU* allowed region in Δm_H vs. Δm_{hS} plane (left panel) and Δm_H vs. α_{HS} plane (right panel) in Case-III with $c_{\beta-\alpha} = \alpha_{hS} = \alpha_{AS} = 0$. In the left panel, α_{HS} is varied to be 0 (blue), $\pi/6$ (orange), and $\pi/4$ (green). In the right panel, Δm_{hS} is varied to be ± 50 GeV (solid and dashed blue) and ± 50 GeV (solid and dashed red). $m_{H^\pm}$ is set to be 800 GeV, and Δm_A is set to be 200 GeV.

$m_{H^\pm} = 800$ GeV and $\Delta m_A = 200$ GeV, with varying $\alpha_{HS} = 0$ (blue), $\pi/6$ (orange), and $\pi/4$ (green). The dashed lines show the approximate relation of $c^2_{\alpha_{HS}}\Delta m_H = -s^2_{\alpha_{HS}}\Delta m_{hS}$ based on Eq. (34). The approximation is valid for Δm_H and Δm_{hS} around a few hundred GeV. As the mass splitting Δm_A increases, the *STU* bands would shrink and be closer to the dashed lines.

In the right panel of Fig. 7, we show the 95% C.L. *STU* allowed region in the Δm_H vs. α_{HS} plane in Case-III for $m_{H^\pm} = 800$ GeV and $\Delta m_A = 200$, with varying $\Delta m_{hS} = \pm 50$ GeV (blue) and 100 GeV (red). Note that the allowed regions are symmetric in α_{HS} and only have a slight variation with respect to the sign of Δm_H.

E. Case-IV: $\alpha_{AS} \neq 0$

In Case-IV, ($\alpha_{AS} \neq 0$ and $c_{\beta-\alpha} = \alpha_{hS} = \alpha_{HS} = 0$), the CP-odd sector has singlet admixture, and the CP-even sector is the same as that in Case-0. The non-zero trilinear Higgs to gauge-boson couplings include

$$c_{A_S HZ}, \quad c_{A_S H^\pm W^\mp}, \tag{35}$$

in addition to those in Eq. (19). Consequently, the couplings involving CP-odd Higgses are parameterized by α_{AS}, *i.e.,* AHZ and $AH^\pm W^\mp$ depend on $c_{\alpha_{AS}}$, and $A_S HZ$ and $A_S H^\pm W^\mp$ depend on $s_{\alpha_{AS}}$. The singlet CP-odd Higgs mass m_{A_S} enters, whereas the CP-even h_S is completely decoupled. In particular, the contribution to the T observable is given by

$$\begin{aligned} T =& \frac{1}{16\pi s_W^2 m_W^2}[c^2_{\alpha_{AS}} F(m^2_{H^\pm}, m^2_A) + s^2_{\alpha_{AS}} F(m^2_{H^\pm}, m^2_{A_S})] \\ &+ F(m^2_{H^\pm}, m^2_H) - [c^2_{\alpha_{AS}} F(m^2_H, m^2_A) + s^2_{\alpha_{AS}} F(m^2_H, m^2_{A_S})], \end{aligned} \tag{36}$$

$$= T_0 + \Delta T_{\rm IV} \tag{37}$$

$$\begin{aligned} \Delta T_{\rm IV} =& \frac{s^2_{\alpha_{AS}}}{16\pi s_W^2 m_W^2}[F(m^2_{H^\pm}, m^2_{A_S}) - F(m^2_H, m^2_{A_S}) \\ &- F(m^2_{H^\pm}, m^2_A) + F(m^2_A, m^2_H)]. \end{aligned} \tag{38}$$

Comparing with Eqs. (29) and (31), we observe that Case-IV is similar to Case-III, with the substitution of H and h_S with A and A_S, as well as the corresponding mass parameters and mixing angles. The approximate expression for T is

$$\begin{aligned} T \approx& \frac{1}{16\pi s_W^2 m_W^2}[F(m^2_{H^\pm}, (c^2_{\alpha_{AS}} m_A + s^2_{\alpha_{AS}} m_{A_S})^2) \\ &- F(m^2_H, (c^2_{\alpha_{AS}} m_A + s^2_{\alpha_{AS}} m_{A_S})^2) + F(m^2_{H^\pm}, m^2_H)], \end{aligned} \tag{39}$$

which leads to a similar approximate mass relation that satisfies the *STU* constraints:

$$c^2_{\alpha_{AS}} m_A + s^2_{\alpha_{AS}} m_{A_S} = m_{H^\pm}, \quad \text{or} \quad m_H = m_{H^\pm}. \tag{40}$$

The 95% C.L. *STU* allowed regions in Δm_H vs. Δm_A, Δm_{AS} vs. Δm_A, and Δm_A vs. α_{AS} are similar to those presented in Figs. 6–7, with the switching of $A \leftrightarrow H$.

In general, the mass splittings of Δm_H and Δm_A can contribute the *STU* observables via the AHZ, $AH^\pm W^\mp$, and $HH^\pm W^\mp$ loops. In the 2HDM+S, the singlet CP-even Higgs h_S can mix with H via the mixing α_{HS}, and the singlet CP-odd Higgs A_S can mix with A_S via α_{AS}. Therefore, Δm_{hS} and Δm_{AS} as well as α_{HS} and α_{AS} enter. The *STU* constraints can be still fulfilled when the mass relations in Eqs. (34) or (40) are satisfied.

V. *STU* CONSTRAINTS BEYOND THE ALIGNMENT LIMIT

For Case-I, we consider the non-alignment limit with all the single mixing angles set to be zero. For Cases-II – IV, we focus on the scenario with only one mixing angle set to be non-zero under the alignment limit. In this section, we consider the cases with a non-zero singlet mixing angle beyond the alignment limit.

We first explore the interplay between $c_{\beta-\alpha}$ with the singlet–h_{125} mixing α_{hS}. In the left plot of Fig. 8, we show the 95% C.L. *STU* allowed region in the m_{h_S} vs. $c_{\beta-\alpha}$ plane for various α_{hS}. For $\alpha_{hS} = 0$ (region enclosed by the solid blue curve), $|c_{\beta-\alpha}|$ is constrained to be less than 0.275, independent of m_{h_S}. However, the singlet admixture can enlarge the allowed region in $|c_{\beta-\alpha}|$, as shown by the two elliptical rings for $\alpha_{hS} = \pi/4$ and $\pi/2$. The $h_S VV$ interaction can compensate for the contribution of $\Delta T_{\rm I}$ in Eq. (24) for larger $|c_{\beta-\alpha}|$.

In the right plot of Fig. 8, we present the 95% C.L. *STU* allowed region in the m_{h_S} vs. α_{hS} plane for various $c_{\beta-\alpha}$. For increasing $|c_{\beta-\alpha}|$, the allowed region shifts to the left. For $m_{h_S} > 125$ GeV, the allowed range of α_{hS} reduces, whereas for $m_{h_S} < 125$ GeV, larger values of α_{hS} are allowed. For $|c_{\beta-\alpha}|$ slightly above 0.275, $\alpha_{hS} = 0$ is no longer allowed, and two branches appear.

We explore the interplay between $c_{\beta-\alpha}$ and singlet-double CP-even Higgs H mixing α_{HS} in Fig. 9. The left panel shows the 95% C.L. *STU* allowed region in the Δm_H vs. $c_{\beta-\alpha}$ plane for $\alpha_{HS} = 0$ (blue), $\pi/4$ (orange), and $\pi/2$ (green). The blue line in the left panel of Fig. 9 is consistent with the blue curve in the left panel of Fig. 4 (Case-I). For larger α_{HS}, the allowed range of $c_{\beta-\alpha}$ shrinks for $\Delta m_H < 0$ but expands for $\Delta m_H > 0$. In this case, $c_{HVV} = c_{\beta-\alpha}c_{\alpha_{HS}}$, $c_{hVV} = s_{\beta-\alpha}$, and $c_{h_S VV} = -c_{\beta-\alpha}s_{\alpha_{HS}}$. As α_{HS} increases, the HVV contribution to the T observable decreases, whereas the $h_S VV$ contribution increases. Therefore, the allowed $c_{\beta-\alpha}$ region shrinks in the $h_S VV$ dominate region ($m_H < m_{h_S}$) and enlarges in the HVV dominate region ($m_H > m_{h_S}$). When $m_H = m_{h_S} = 800$ GeV,

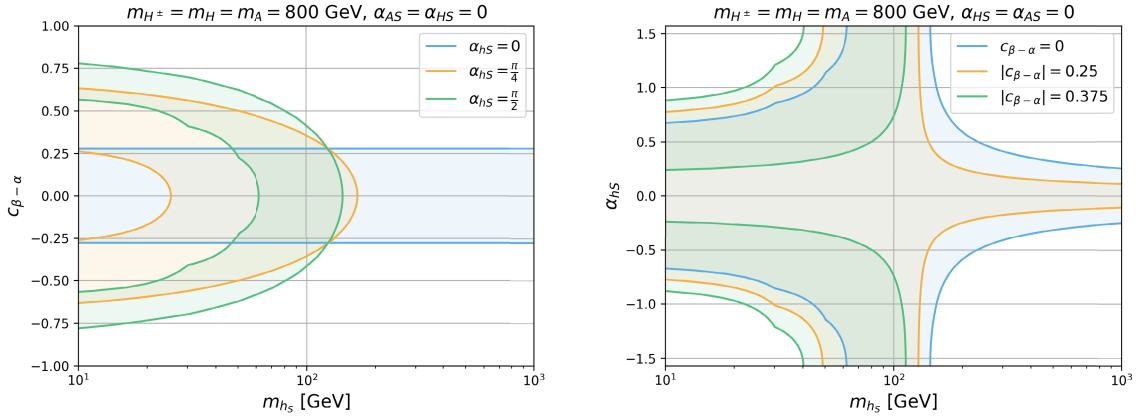

Fig. 8. (color online) 95% C.L. *STU* allowed region in the m_{h_S} vs. $c_{\beta-\alpha}$ plane (left panel) for $\alpha_{hS} = 0$ (blue), $\pi/4$ (orange), and $\pi/2$ (green) and the m_{h_S} vs. α_{hS} plane (right panel) for $c_{\beta-\alpha} = 0$ (blue), 0.25 (orange), and 0.375 (green). We set $m_{H^\pm} = m_H = m_A = 800$ GeV and $\alpha_{AS} = \alpha_{HS} = 0$.

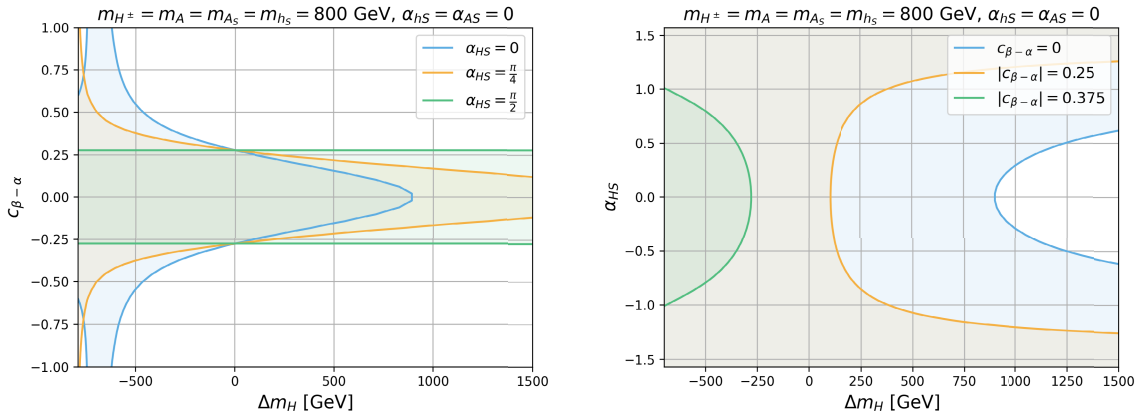

Fig. 9. (color online) 95% C.L. *STU* allowed region in the Δm_H vs. $c_{\beta-\alpha}$ plane (left panel) for α_{HS}=0 (blue), $\pi/4$ (orange), and $\pi/2$ (green) and the Δm_H vs. α_{HS} plane (right panel) for $|c_{\beta-\alpha}|$=0 (blue), 0.25 (orange), and 0.375 (green). We set $m_{H^\pm} = m_A = m_{h_S} = m_{A_S} = 800$ GeV and $\alpha_{AS} = \alpha_{hS} = 0$.

the $h_S VV$ term plays the same role as HVV. The STU constraints of this point are independent of α_{HS} and all curves cross at $\Delta m_H = 0$. For $\alpha_{HS} = \pi/2$, H becomes the pure singlet Higgs and does not contribute to the STU parameters. Therefore, the STU limit of $|c_{\beta-\alpha}| < 0.275$ is independent of m_H. As the roles of H and h_S switch when $\alpha_{HS} \to \pi/2 - \alpha_{HS}$, the parameter space of $c_{\beta-\alpha}$ vs. Δm_{h_S} is the same as that of the left panel of Fig. 9 with $\alpha_{HS} \to \pi/2 - \alpha_{HS}$.

The right panel of Fig. 9 presents the Δm_H vs. α_{HS} plane for $|c_{\beta-\alpha}|$=0 (blue), 0.25 (orange), and 0.375 (green). For $c_{\beta-\alpha} = 0$, almost the entire region of the parameter space is allowed, except for a small open region with relatively small α_{HS} and large Δm_H. The allowed region reduces when $|c_{\beta-\alpha}|$ increases. For $|c_{\beta-\alpha}| = 0.375$, only a small region with $\Delta m_H < -250$ GeV and $|\alpha_{HS}| < 1$ is allowed. This is due to the increased contribution from the HVV term at larger $|c_{\beta-\alpha}| = 0.375$. Only when m_H is lighter and close to 125 GeV would the HVV contribution be small enough to be allowed. Similar to the left panel, the parameter space of α_{HS} vs. Δm_{h_S} is the same as that of the right panel of Fig. 9 with $\alpha_{HS} \to \pi/2 - \alpha_{HS}$.

We explore the interplay between $c_{\beta-\alpha}$ and singlet-double CP-odd Higgs A mixing α_{AS} in Fig. 10. The left panel presents the 95% C.L. allowed region in Δm_A vs. $c_{\beta-\alpha}$ for α_{HS}=0 (blue), $\pi/4$ (orange), and $\pi/2$ (green). The blue region in the left panel of Fig. 10 for $\alpha_{AS} = 0$ is consistent with the blue region in the right panel of Fig. 4. For larger α_{AS}, the allowed regions shift to the left, whereas the $c_{\beta-\alpha}$ bounds at both $m_A > m_{A_S}$ and $m_A < m_{A_S}$ become larger, owing to the suppression of both the AHZ and AhZ terms by $c_{\alpha_{AS}}$. However, the $A_S hZ$ term is enhanced by $s_{\alpha_{AS}}$, which compensates for the suppression of AHZ and AhZ. Therefore, the STU limit is relaxed faster at $m_A > m_{A_S}$ where A_S is less dominant in this region. For $\alpha_{AS} = \pi/2$, only the $A_S hZ$ contribution is left, and the contribution from A is decoupled. The 95% C.L. allowed region for the $c_{\beta-\alpha}$ limit is a constant and independent of m_A. As the roles of A and A_S switch when $\alpha_{AS} \to \pi/2 - \alpha_{AS}$, the parameter space of $c_{\beta-\alpha}$ vs. Δm_{A_S} is the same as that in the left panel of Fig. 10 with $\alpha_{AS} \to \pi/2 - \alpha_{AS}$.

The right panel of Fig. 10 presents the 95% C.L. al-

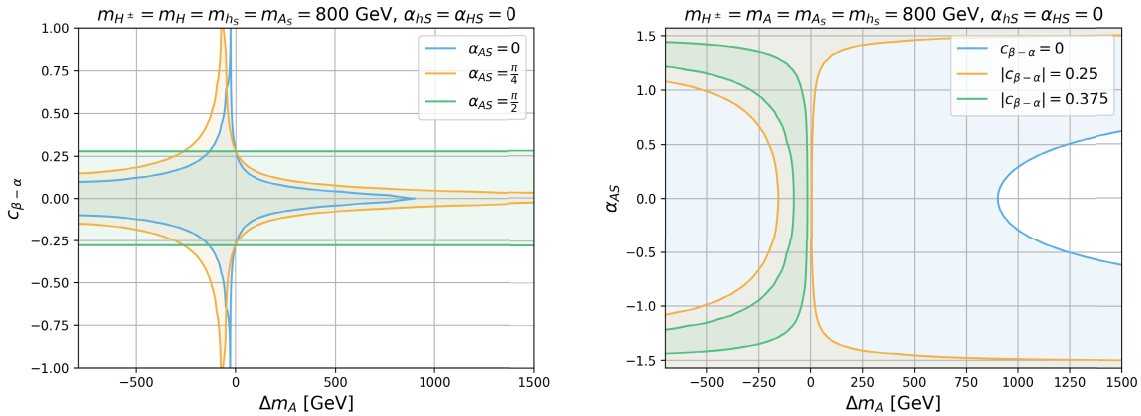

Fig. 10. 95% C.L. *STU* allowed region in the Δm_A vs. $c_{\beta-\alpha}$ plane (left panel) for α_{HS}=0 (blue), $\pi/4$ (orange), and $\pi/2$ (green) and the Δm_A vs. α_{AS} plane (right panel) for $|c_{\beta-\alpha}|$=0 (blue), 0.25 (orange), and 0.375 (green). We set $m_{H^\pm} = m_H = m_{h_S} = m_{A_S} = 800$ GeV and $\alpha_{hS} = \alpha_{HS} = 0$.

lowed region in Δm_A vs. α_{AS} for $|c_{\beta-\alpha}|$=0 (blue), 0.25 (orange), and 0.375 (green). The blue line indicates the same behavior of the *STU* dependence on (m_A, α_{AS}) as (m_H, α_{HS}) for $c_{\beta-\alpha} = 0$. However, these two cases differ when singlet admixture enters for $c_{\beta-\alpha} \neq 0$. The CP-odd Higgs A enters via AhZ and AHZs, where these contributions are suppressed when m_A is close to m_H. In the case where $m_{A_S} = m_H$, the allowed regions that only appear in the region of large α_{AS} are non-zero Δm_A, as A_S in this area is already dominated by the doublet properties. Similar to the left panel, the parameter space of α_{AS} vs. Δm_{A_S} is the same as that in the right panel of Fig. 10 with $\alpha_{AS} \to \pi/2 - \alpha_{AS}$.

VI. INTERPLAY OF ELECTROWEAK AND HIGGS PRECISION MEASUREMENTS

The precision measurements of the couplings of the 125 GeV Higgs at the LHC also place strong constraints on the parameter space of the 2HDM+S, in particular, on $c_{\beta-\alpha}$, the singlet-h_{125} mixing α_{hS}, and $\tan\beta$. We perform the fit for 125 GeV Higgs properties with `HiggsTools` [31−35]. In Fig. 11, we present both the 95% C.L. *STU* allowed region in the $c_{\beta-\alpha}$ vs. α_{hS} plane for various m_{h_S} (regions enclosed by solid curves) and the 95% C.L. allowed region by 125 GeV Higgs precision measurements for various $\tan\beta$ (region enclosed by dashed curves) for Type-I (left panel) and Type-II (right panel). As the *STU* constraints only depend on the couplings of the Higgses with the gauge bosons, which is the same for different types of 2HDM, the solid curves are the same at both panels. For $m_{h_S} = 125$ GeV, the allowed range in $c_{\beta-\alpha}$ is independent of α_{hS}. This is because $h_S VV$ and hVV contribute the same for $m_h = m_{h_S}$, and α_{hS} is not constrained as shown in the left plot of Fig. 5. For $m_{h_S} = 50$ GeV, a larger region of $c_{\beta-\alpha}$ can be accommodated for $\alpha_{h_S} \neq 0$, as a larger $\Delta T_{\rm I}$ can be compensated for by $h_S VV$ with light-

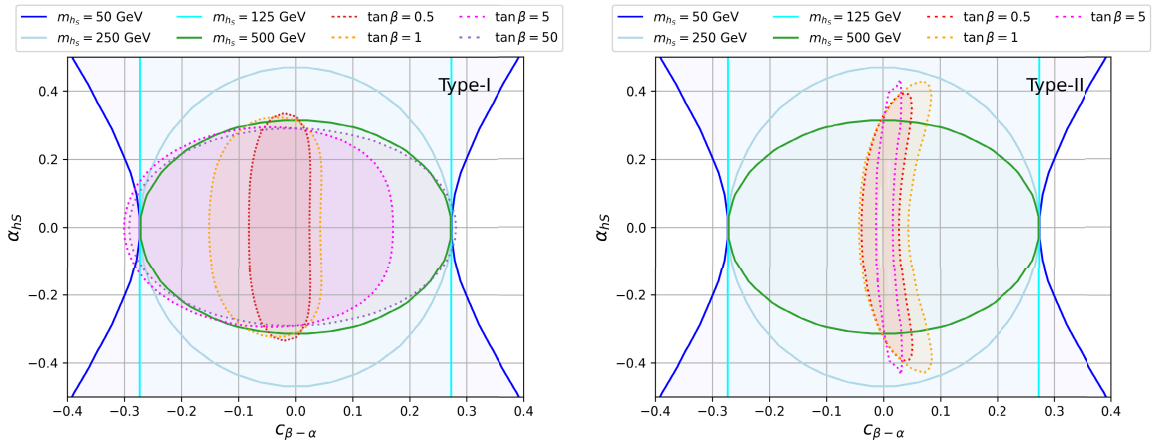

Fig. 11. Parameter space of $c_{\beta-\alpha}$ vs. α_{hS} for m_{h_S} =50 GeV (dark blue), 125 GeV (cyan), 250 GeV (light blue), and 500 GeV (green) and $\tan\beta$ =0.5 (red), 1 (orange), 5 (magenta), and 50 (purple) under electroweak precision measurements (solid curves) and Higgs precision measurements (dashed curves). The other Higgs masses are $m_A = m_H = m_{H^\pm} = 800$ GeV, and $\alpha_{HS} = \alpha_{AS} = 0$. The left panel indicates the type-I 2HDM+S, and the right panel indicates the type-II 2HDM+S.

er m_{h_S}. In contrast, for $m_{h_S} > 125$ GeV, the allowed region in α_{h_S} shrinks, where $\Delta T_{\rm I}$ and $h_S VV$ have the same sign in this mass region, which leads to tighter constraints.

For the Higgs precision on the Type-I 2HDM+S in the left panel, the allowed range of $c_{\beta-\alpha}$ becomes weaker for larger $\tan\beta$. For $\tan\beta \gtrsim 5$, the electroweak precision measurements provide a stronger constraint on $c_{\beta-\alpha}$ in the negative $c_{\beta-\alpha}$ region, whereas the Higgs precision measurements constrain the value of α_{h_S} better for $m_{h_S} \lesssim 500$ GeV. For $\tan\beta \sim 50$, the *STU* constraint on positive $c_{\beta-\alpha}$ can be stronger than the Higgs precision measurement at $\alpha_{hS} \sim 0$. Thus, $|\alpha_{hS}|$ in the Type-I model would be constrained to be less than 0.3 by the h_{125} coupling measurements, where the *STU* can provide a stronger α_{hS} limit for $m_{h_S} > 500$ GeV.

For the Higgs precision on the Type-II 2HDM+S in the right panel, the allowed region in $c_{\beta-\alpha}$ is constrained to be much tighter, to only a thin region around $c_{\beta-\alpha} \sim 0$. The constraints from the h_{125} coupling measurements are the weakest at $\tan\beta \sim 1$ and become stronger as $\tan\beta$ increases or decreases. $|\alpha_{hS}|$ is constrained to be approximately 0.4, which is less dependent on the values of $\tan\beta$. The electroweak precision measurements provide a tight bound on the range of α_{hS} for $m_{h_S} > 250$ GeV. A combination of the electroweak precision measurements and the Higgs precision measurements could help us narrow down the parameter space of the 2HDM+S.

VII. CONCLUSIONS

We studied the implications of the oblique parameters, in particular, the *T* parameter, on the parameter space of the 2HDM+S model. Nine model parameters enter, including five masses m_H, m_{h_S}, m_A, m_{A_S}, and $m_{H^\pm}$ and four mixing angles $c_{\beta-\alpha}$, α_{hS}, α_{HS}, and α_S. To systematically study the impact of each mixing angle, we identified five benchmark scenarios, Case-0 with $c_{\beta-\alpha} = 0$ and all the singlet mixing angles being 0 (the 2HDM alignment limit), and Cases-I to IV with only one of the mixing angles being non-zero. We studied the 95% C.L. *STU* allowed region in the relevant parameter spaces. We observed that

● **Case-0**

Other than the well known conclusion that the electroweak precision constraints are satisfied for $\Delta m_H = 0$ or $\Delta m_A = 0$, there is an upper limit on the mass splitting of $\Delta m_{H/A} \lesssim 900$ GeV for $m_{H^\pm} = 800$ GeV and $\Delta m_{A,H} = 0$, coming from the *S* parameter constraint. This upper limit also varies with $m_{H^\pm}$.

● **Case-I with** $c_{\beta-\alpha} \neq 0$

The constraint on $c_{\beta-\alpha}$ is weak for $m_H = 125$ GeV, $\Delta m_A = 0$, or $m_H = m_{H^\pm}$ and $\Delta m_A \sim -30$ GeV. The parameter space in $\Delta m_H - c_{\beta-\alpha}$ or $\Delta m_A - c_{\beta-\alpha}$ is significantly reduced for Δm_A or Δm_H away from 0.

● **Case-II with** $\alpha_{hS} \neq 0$

α_{hS} is unconstrained for $m_{h_S} = 125$ GeV and $\Delta m_{H,A} = 0$. The allowed region shifts to larger m_{h_S} and $|\alpha_{hS}|$ for $\Delta m_{A,H} \neq 0$.

● **Case-III with** $\alpha_{HS} \neq 0$

The *STU* constraint can be satisfied for $c^2_{\alpha_{HS}} m_H + s^2_{\alpha_{HS}} m_{h_S} = m_{H^\pm}$ or $m_A = m_{H^\pm}$.

● **Case-IV with** $\alpha_{AS} \neq 0$

The *STU* constraint can be satisfied for $c^2_{\alpha_{AS}} m_A + s^2_{\alpha_{AS}} m_{A_S} = m_{H^\pm}$ or $m_H = m_{H^\pm}$.

We further explored Cases-II–IV with non-zero $c_{\beta-\alpha}$ and observed that the singlet extension could compensate for the $c_{\beta-\alpha}$ contribution and extend the allowed parameter space. However, a larger $|c_{\beta-\alpha}|$ typically leads to more constrained mass vs. mixing angle parameter space.

We also studied the complementarity between the electroweak precision analyses and Higgs coupling measurements. We observed that, for the Type-I scenario, the electroweak precision measurements provide stronger constraints on α_S for $m_{hS} > 500$ GeV, whereas the Higgs coupling measurements constrain $c_{\beta-\alpha}$ better for $\tan\beta > 5$. For the Type-II scenario, the electroweak precision measurements provide a tight bound on the range of α_{hS} for $m_{h_S} > 250$ GeV, whereas the Higgs coupling measurements constrain $c_{\beta-\alpha}$ better for all values of $\tan\beta$.

In summary, the singlet extension of the 2HDM opens up the allowed parameter space when constraints from the electroweak precision measurements are considered. It also provides a complementary reach when combined with Higgs precision measurements. While our study examined benchmark scenarios with only one singlet mixing angle being nonzero, it identified the main features of each mixing case and provided a more comprehensive understanding in the most general mixing cases. Note that we adopted the set of the model parameters including physical Higgs masses and mixing angles. When studying a particular 2HDM+S scenario with a specific symmetry assumption of the Higgs potential, theoretical considerations might restrict the range of the mixing angles and mass differences. Our analyses were performed in a model independent way so that it is straightforward to map our results to a particular 2HDM+S model with a restricted range of mixing angles and mass differences.

APPENDIX A

The *STU* observables are defined by

$$\alpha(m_Z)T = \frac{\Pi_{WW}(0)}{m_W^2} - \frac{\Pi_{ZZ}(0)}{m_Z^2}, \tag{A1}$$

$$\frac{\alpha(m_Z)}{4s_W^2c_W^2}S = \frac{\Pi_{ZZ}(m_Z^2)-\Pi_{ZZ}(0)}{m_Z^2} - \frac{c_W^2-s_W^2}{s_Wc_W}\frac{\Pi_{Z\gamma}(m_Z^2)}{m_Z^2} - \frac{\Pi_{\gamma\gamma}(m_Z^2)}{m_Z^2}, \tag{A2}$$

$$\frac{\alpha(m_Z)}{4s_W^2}(S+U) = \frac{\Pi_{WW}(m_W^2)-\Pi_{WW}(0)}{m_W^2} - \frac{c_W}{s_W}\frac{\Pi_{Z\gamma}(m_Z^2)}{m_Z^2} - \frac{\Pi_{\gamma\gamma}(m_Z^2)}{m_Z^2}, \tag{A3}$$

where the F, G, and $\hat{G}$ functions are defined as [22]

$$F(I,J) = \begin{cases} \frac{I+J}{2} - \frac{IJ}{I-J}\ln\frac{I}{J} & \text{for } I \neq J, \\ 0 & \text{for } I = J. \end{cases} \tag{A4}$$

$$G(I,J,Q) = -\frac{16}{3} + \frac{5(I+J)}{Q} - \frac{2(I-J)^2}{Q^2} + \frac{r}{Q^3}f(I+J-Q, Q^2-2Q(I+J)+(I-J)^2) + \frac{3}{Q}\left[\frac{I^2+J^2}{I-J} - \frac{I^2-J^2}{Q} + \frac{(I-J)^3}{3Q^2}\right]\ln\frac{I}{J}, \tag{A5}$$

$$\hat{G}(I,Q) = -\frac{79}{3} + 9\frac{I}{Q} - 2\frac{I^2}{Q^2} + \left(12 - 4\frac{I}{Q} + \frac{I^2}{Q^2}\right)\frac{f(I,I^2-4IQ)}{Q} + \left(-10 + 18\frac{I}{Q} - 6\frac{I^2}{Q^2} + \frac{I^3}{Q^3} - 9\frac{I+Q}{I-Q}\right)\ln\frac{I}{Q}. \tag{A6}$$

with

$$f(r,t) = \begin{cases} \sqrt{r}\ln\left|\frac{t-\sqrt{r}}{t+\sqrt{r}}\right| & \text{for } r > 0, \\ 0 & \text{for } r = 0, \\ 2\sqrt{-r}\arctan\frac{\sqrt{-r}}{t} & \text{for } r < 0. \end{cases} \tag{A7}$$

References

[1] G. P. Salam, L. T. Wang, and G. Zanderighi, Nature **607**(7917), 41 (2022), arXiv: 2207.00478
[2] J. Gu, H. Li, Z. Liu *et al.*, JHEP **12**, 153 (2017), arXiv: 1709.06103
[3] G. Aad *et al.* (ATLAS Collaboration), Phys. Lett. B **716**, 1 (2012), arXiv: 1207.7214
[4] S. Chatrchyan *et al.* (CMS Collaboration), Phys. Lett. B **716**, 30 (2012), arXiv: 1207.7235
[5] A. Crivellin and B. Mellado, Nature Rev. Phys. **6**(5), 294 (2024), arXiv: 2309.03870
[6] H. Georgi, H. R. Quinn, and S. Weinberg, Phys. Rev. Lett. **33**, 451 (1974)
[7] A. G. Cohen, D. B. Kaplan, and A. E. Nelson, Ann. Rev. Nucl. Part. Sci. **43**, 27 (1993), arXiv: hep-ph/9302210
[8] G. Bertone, D. Hooper, and J. Silk, Phys. Rept. **405**, 279 (2005), arXiv: hep-ph/0404175
[9] S. P. Martin, Adv. Ser. Direct. High Energy Phys. **18**, 1 (1998), arXiv: hep-ph/9709356
[10] G. C. Branco, P. M. Ferreira, L. Lavoura *et al.*, Phys. Rept. **516**, 1 (2012), arXiv: 1106.0034
[11] M. Muhlleitner, M. O. P. Sampaio, R. Santos *et al.*, JHEP **03**, 094 (2017), arXiv: 1612.01309
[12] A. Arhrib, R. Benbrik, M. El Kacimi *et al.*, Eur. Phys. J. C **80**(1), 13 (2020), arXiv: 1811.12431
[13] T. Biekötter, M. Chakraborti, and S. Heinemeyer, Eur. Phys. J. C **80**(1), 2 (2020), arXiv: 1903.11661
[14] S. Baum and N. R. Shah, JHEP **12**, 044 (2018), arXiv: 1808.02667
[15] S. Heinemeyer, C. Li, F. Lika *et al.*, Phys. Rev. D **106**(7), 075003 (2022), arXiv: 2112.11958
[16] U. Ellwanger, C. Hugonie, and A. M. Teixeira, Phys. Rept. **496**, 1 (2010), arXiv: 0910.1785
[17] J. Dutta, G. Moortgat-Pick, and M. Schreiber, Eur. Phys. J. Plus **140**(1), 87 (2025), arXiv: 2203.05509
[18] J. Dutta, J. Lahiri, C. Li *et al.*, Eur. Phys. J. C **84**(9), 926 (2024), arXiv: 2308.05653
[19] J. Dutta, J. Lahiri, C. Li *et al.*, *Search for Dark Matter in 2HDMS at LHC and future Lepton Colliders*, arXiv: 2504.14529
[20] M. E. Peskin and T. Takeuchi, Phys. Rev. Lett. **65**, 964 (1990)
[21] M. E. Peskin and T. Takeuchi, Phys. Rev. D **46**, 381 (1992)
[22] W. Grimus, L. Lavoura, O. M. Ogreid *et al.*, Nucl. Phys. B **801**, 81 (2008), arXiv: 0802.4353
[23] D. Toussaint, Phys. Rev. D **18**, 1626 (1978)
[24] A. Pomarol and R. Vega, Nucl. Phys. B **413**, 3 (1994), arXiv: hep-ph/9305272
[25] H. E. Haber and D. O'Neil, Phys. Rev. D **83**, 055017 (2011), arXiv: 1011.6188
[26] J. Haller, A. Hoecker, R. Kogler *et al.*, Eur. Phys. J. C **78**(8), 675 (2018), arXiv: 1803.01853
[27] V. Barger, P. Langacker, M. McCaskey *et al.*, Phys. Rev. D **77**, 035005 (2008), arXiv: 0706.4311
[28] J. Erler and A. Freitas, *Electroweak model and constraints on new physics*, *pdg.lbl.gov/2024/reviews/rpp2024-rev-standard-model*, (2024)
[29] M. Baak *et al.* (Gfitter Collaboration), Eur. Phys. J. C **72**,

2003 (2012), arXiv: 1107.0975
[30] M. Gorbahn, J. M. No, and V. Sanz, JHEP **10**, 036 (2015), arXiv: 1502.07352
[31] H. Bahl, T. Biekötter, S. Heinemeyer *et al*., Comput. Phys. Commun. **291**, 108803 (2023), arXiv: 2210.09332
[32] P. Bechtle, S. Heinemeyer, O. Stål *et al*., Eur. Phys. J. C **74**(2), 2711 (2014), arXiv: 1305.1933
[33] O. Stål and T. Stefaniak, PoS **EPS-HEP2013**, 314 (2013), arXiv: 1310.4039
[34] P. Bechtle, S. Heinemeyer, O. Stål *et al*., JHEP **11**, 039 (2014), arXiv: 1403.1582
[35] P. Bechtle, S. Heinemeyer, T. Klingl *et al*., Eur. Phys. J. C **81**(2), 145 (2021), arXiv: 2012.09197